JOURNAL OF THERMOPHYSICS AND HEAT TRANSFER
Vol. 19, No. 4, October–December 2005

Analysis of Supercritical Startup of Cryogenic Heat Pipes with Parasitic Heat Loads

Paulo Couto*
Federal University of Rio de Janeiro, 21945-970 Rio de Janeiro, Brazil
Jay M. Ochterbeck†
Clemson University, Clemson, South Carolina 29631
and
Marcia B. H. Mantelli‡
Federal University of Santa Catarina, 88040-900 Florianopolis, Brazil

A mathematical model to predict the transient temperature profile of a cryogenic heat pipe during startup is presented. The improved model accounts for a known time-variable temperature boundary condition at the condenser region, while the boundary condition in the remaining length of the heat pipe is a radiative parasitic heat flux. The vapor pressure is modeled to determine the mass distribution of the saturated liquid inside the heat pipe. An axially grooved aluminum/oxygen cryogenic heat pipe is considered. Theoretical results for the axial temperature profile of the heat pipe for the startup period are compared to experimental μ-*g* flight data to validate the new model. Following the validation, the effects of some operational parameters over the axial temperature profile for the startup period are investigated to determine under what conditions the cryogenic heat pipe will start properly.

Nomenclature

A	=	area, m^2
a	=	constant coefficients
b	=	constant coefficient
C_{eff}	=	effective volumetric heat capacity
c	=	specific heat, $J/kg \cdot K$
$F_{\text{cap,fric}}$	=	driving forces (cap = capillary, fric = frictional), N
$F_{\text{HP},\infty}$	=	view factor between heat pipe and environment
h	=	groove depth, m
h_{fg}	=	latent heat, J/kg
K	=	permeability, m^2
k	=	thermal conductivity, $W/m \cdot K$
L	=	length, m
m	=	working fluid mass, kg
$\dot{m}$	=	mass flow rate, kg/s
$\dot{m}_{\text{evap}}$	=	mass flow rate evaporated, kg/s
N	=	liquid fill rate
n	=	quality
P	=	pressure, kPa
q_p	=	parasitic heat load, W
q''_p	=	parasitic heat flux, W/m^2
R_g	=	gas constant, $J/kg \cdot K$
r	=	radius, m
s	=	liquid column length, m
T	=	temperature, K
T_{crit}	=	critical temperature of the working fluid, K
T_{HP}	=	temperature of an isothermal heat pipe, K
T_{op}	=	heat pipe operational temperature, K
T_0	=	initial temperature, K
T_∞	=	surrounding temperature, K
t	=	time, s
U	=	average liquid velocity, m/s
U_r	=	rewetting velocity, m/s
V	=	volume, m^3
v	=	specific volume
w	=	groove width, m
x	=	axial coordinate, m
Z	=	compressibility factor
α_{eff}	=	effective thermal diffusivity, m^2/s
$\bar{\alpha}$	=	residual Helmholtz energy
β	=	constant coefficient
ΔE	=	total internal energy variation, kJ
δ	=	wall thickness, m
ε	=	surface emissivity
μ	=	dynamic viscosity, $N \cdot s/m^2$
ρ	=	density, kg/m^3
$\bar{\rho}$	=	reduced density
σ	=	surface tension, N/m
σ_r	=	Stefan–Boltzmann constant, W/m^2K^4
φ	=	porosity

Subscripts

c	=	condenser section
crit	=	critical point thermodynamic properties
e	=	exposed area of the heat pipe (evaporator + adiabatic)
eff	=	effective properties
f	=	supercritical/super-heated fluid
ℓ	=	liquid layer, liquid thermodynamic properties
s	=	solid wall, solid thermodynamic properties
sat	=	thermodynamic properties in the saturation region
v	=	vapor layer, vapor thermodynamic properties
w	=	wick region

Presented as Paper 2002-3095 at the AIAA/ASME 8th Joint Thermophysics and Heat Transfer Conference, St. Louis, MO, 24–26 June 2002; received 14 May 2004; revision received 19 January 2005; accepted for publication 21 February 2005.

*Associate Research Engineer, P.O. Box 68503, Department of Mechanical Engineering—POLI/COPPE; pcouto@lttc.coppe.ufrj.br. Member AIAA.

†Professor, Department of Mechanical Engineering; jochter@ces.clemson.edu. Associate Fellow AIAA.

‡Professor, Department of Mechanical Engineering—LABSOLAR/NCTS; marcia@emc.ufsc.br. Member AIAA.

Introduction

IN 1996, the Satellite Thermal Control Laboratory (NCTS/UFSC) began the development of a Passive Cryogenic Radiator[1] in the framework of the University Program for Space Development,

funded by the Brazilian Space Agency. Passive cryogenic radiators are used to cool equipment, such as infrared sensors and charge-coupled-device cameras, to the cryogenic temperature levels required for optimum operation. However, in many satellite designs, the equipment to be cooled cannot be placed near the heat sink. Usually, cryogenic heat pipes are used to transfer heat from the equipment to the heat sink.[2–5] In addition, cryogenic heat pipes are used in the thermal control of focal planes of infrared sensors,[6] X-ray telescopes,[7] and in the cooling of superconducting magnets.[8] The design of cryogenic heat pipes is now under investigation at the NCTS/ UFSC[9] in order to develop a passive cryogenic thermal control device for payloads of the Brazilian satellites, described at the Brazilian Policy for Space Activities.[10]

Cryogenic heat pipes operate at temperatures below 200 K, which makes this system very sensitive to heat leaks from the surrounding environment (e.g., satellite structure). The parasitic heat loads can change significantly the operational temperature of the cryogenic heat pipe and can add loads to the heat pipe on the order of the maximum transport capability. In addition to imposing additional heat load, the parasitic heat leaks can adversely affect the transient startup behavior for the system. Additionally, the operational temperature range of cryogenic heat pipes is relatively narrow.[11–13] For the development and testing of cryogenic heat pipes, the transient response of the heat pipe temperature must be well known.

Literature Review

Unlike low- and medium-temperature heat pipes, a cryogenic heat pipe typically starts from a supercritical state. The entire heat pipe must be cooled below the saturation temperature of the working fluid before nominal operation begins. Previously, Colwell,[14] Brennan et al.,[15] Rosenfeld et al.,[16] and Yan and Ochterbeck[17] have discussed the startup process of cryogenic heat pipes.

Colwell[14] presented a numerical analysis of the transient behavior of a nitrogen/stainless-steel cryogenic heat pipe with circumferential screen wick structure and composite central slab. The three-dimensional model assumed constant properties, but did not account for the fluid dynamics of the working fluid. Although provisions for simulating a supercritical startup were listed, the author only presented results for the startup of the heat pipe with an initial temperature already below the critical temperature of the working fluid.

A microgravity experiment for two different aluminum/oxygen axially grooved heat pipes was conducted by Brennan et al.[15] The experiment was flown aboard the STS-53 space shuttle mission in December 1992. Reliable startups in flight of the two heat pipes were performed, but the startup process in microgravity was slower than that obtained in ground tests. This is because in a microgravity environment any excess liquid condensate of the working fluid develops a liquid slug in the condenser region. In ground tests the excess of liquid spreads along the top of the wick structure because of the effects of the gravitational forces. In this case, the liquid typically forms a puddle as a result of the very low surface tension of cryogenic fluids.

Rosenfeld et al.[16] presented a study of the supercritical startup of a titanium/nitrogen heat pipe. The test was performed during mission STS-62 (March 1994). This heat pipe reached a nonoperational steady-state thermal condition during microgravity tests. Only 30% of the heat-pipe length cooled below the nitrogen critical point, but the vapor pressure was still above the critical pressure. However, Rosenfeld et al.[16] observed that in ground tests the titanium/nitrogen heat pipe underwent startup successfully. The authors concluded that, with the addition of parasitic heat loads, the axial thermal conduction of the titanium/nitrogen heat pipe was insufficient to decrease the axial temperature profile in order to allow for the internal pressure to decrease below the critical pressure of nitrogen when in microgravity. The successful startup during ground tests was caused by enhanced thermal transport of the gravity-assisted excess liquid "puddling" effects. These tests highlighted the significance of the parasitic heat loads, as the heat-pipe startup failure would not have occurred in microgravity if the heat leaks had been significantly reduced.

Yan and Ochterbeck[17] presented a one-dimensional transient model for the supercritical startup of cryogenic heat pipes. The startup process was summarized into two stages. In the first stage, the heat pipe is cooled by pure heat conduction, and the vapor temperature at the condenser and pressure are greater than the critical temperature and pressure ($T_c > T_{\text{crit}}$ or $P > P_{\text{crit}}$). The cooling effect resulting from the condenser heat rejection is not immediately propagated through the heat pipe, but it is confined to a region extending from the condenser to some penetration depth δ. Beyond δ, the temperature gradient is zero. When the penetration depth equals the heat-pipe length, the cooling effect of the condenser has propagated over the entire heat pipe.

In the second stage, the vapor temperature and pressure are lower than the critical temperature and pressure ($T_c < T_{\text{crit}}$ and $P < P_{\text{crit}}$). When the condenser temperature is lower than the critical temperature and the internal pressure is lower than the critical point, the vapor begins to condense in the condenser section. The advancing liquid layer is subjected to a capillary driving force that is induced by surface tension and opposed by the wall shear stress, as it advances with a velocity that will vary with respect to the length of the liquid layer. With increasing time, the liquid velocity in the condenser increases. The liquid front will advance, until the heat pipe reaches its operational steady state, assuming sufficiently low heat leaks. This model compared favorably with the microgravity experimental data presented by Brennan et al.,[15] but it did not include the effects of parasitic heat loads on the heat-pipe working fluid.

In the current work, provisions to account for the parasitic heat load during the supercritical startup of cryogenic heat pipes are included in the model of Yan and Ochterbeck.[17] Also, a methodology to determine the vapor pressure and working fluid mass distribution in the wick and vapor regions are included, which allows for the determination of the length of the liquid slug in microgravity.

Analysis

The supercritical startup of cryogenic heat pipes is considered for both axially grooved and porous sintered metal wick. The initial temperature of the heat pipe T_0 is above the critical temperature, and the boundary condition at the condenser region is a specified time-variable temperature. This condition is consistent with most experiments in the literature,[14–16] which use cryocoolers to provide the required heat rejection at the condenser region. The remaining length of the heat pipe (transport and evaporator regions) is considered to be under the influence of a radiative parasitic heat load. This parasitic heat load is provided by the radiation heat transfer between the heat pipe and the spacecraft structure and heat loads from the space environment (e.g., direct sun irradiation, Earth emission, albedo, etc.). Also the vapor pressure and density gradient of the working fluid are determined based on the temperature gradient and the total working fluid mass. Figure 1 shows the schematic of the physical model, as well as the boundary conditions and the coordinate system.

Thermodynamic Analysis

Depending on the initial condition of the heat pipe, the working fluid at the condenser region can achieve a subcooled condition prior to that of a saturated condition. The current analysis considers two cases for the initial condition: the initial specific volume of the

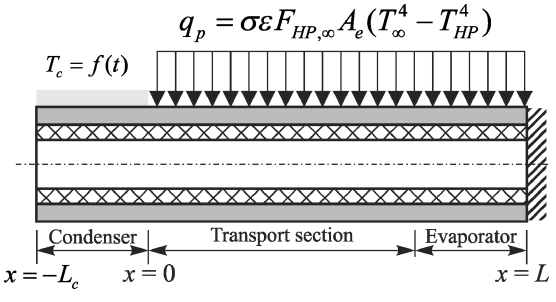

Fig. 1 Physical model and coordinate system (first stage of startup).

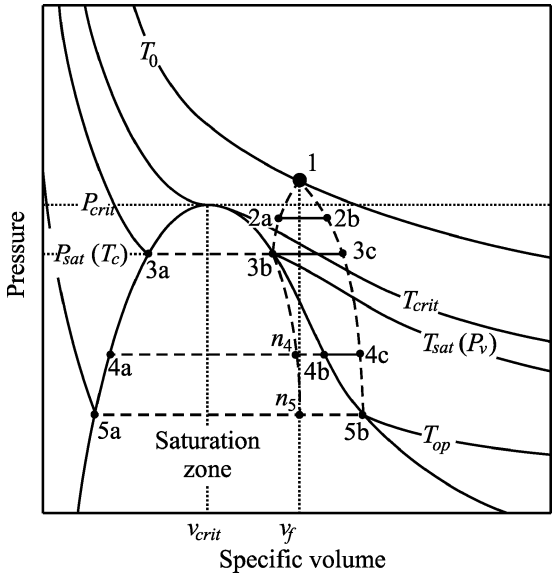

Fig. 2 Pressure-specific volume diagram for $v_f \gg v_{crit}$.

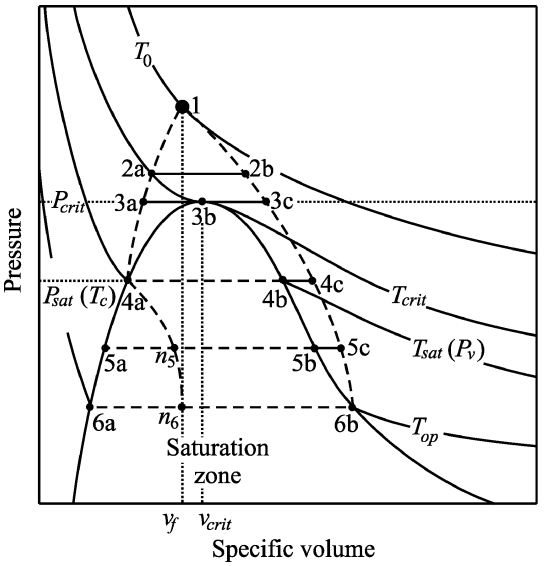

Fig. 3 Pressure-specific volume diagram for $v_f < v_{crit}$.

heat-pipe's working fluid (void volume of the heat-pipe/working fluid mass) is much larger than the critical specific volume of the working fluid ($v_f \gg v_{crit}$), or the specific volume is less or near the critical specific volume ($v_f < v_{crit}$ or $v_f \sim v_{crit}$).

Case 1: $v_f \gg v_{crit}$

The first case can be understood by observing the pressure-specific volume diagram shown in Fig. 2. At the beginning of the process, the heat pipe is considered to be isothermal at T_0, where the initial condition of the heat pipe is represented by point 1 in the supercritical region. As the startup proceeds, a horizontal line represents the thermodynamic state of the heat pipe, where the pressure is assumed essentially uniform in the heat pipe at any point in time. This line lowers as the pressure of the vapor decreases. In Fig. 2, point 2a represents the specific volume at the condenser end, and point 2b represents the specific volume at the evaporator end. It is important to observe, at the thermodynamic state 2, that the vapor pressure is lower than the critical pressure, but the temperature of the condenser might remain above the critical temperature. As the temperature of the condenser continues to decrease, the condenser will enter the superheated region when the temperature of the condenser decreases below the critical temperature, or $T_c < T_{crit}$. The condensation process will start when the temperature of the condenser equals the saturation temperature (point 3b) at the vapor pressure at that point in time [$T_c = T_{sat}(P_v) \equiv P_v = P_{sat}(T_c)$]. In this moment, liquid condenses at the wick structure (point 3a), and saturated vapor fills the vapor space at the condenser region (point 3b). The remaining length of the heat pipe remains dry in a superheated condition (line 3b–3c). As the temperature of the condenser continues to decrease (line 4a–4b–4c), more liquid condenses along the wick structure and forms a liquid column, which eventually advances towards the evaporator. The process continues until the heat pipe is completely primed (assuming parasitic heat leaks are not greater than the maximum transport capacity), and the thermodynamic state at the wick structure and vapor space is given by points 5a and 5b, respectively. This case primarily is theoretical and is not easily realized in practice, as the necessary volume of the vapor space would be orders of magnitude greater than the volume of liquid, which is typically not the case in actual heat pipes.

Case 2: $v_f < v_{crit}$ *or* $v_f \sim v_{crit}$

The second case, which represents the majority of practical applications, can be understood by observing the pressure-specific volume diagram shown in Fig. 3 and the thermodynamic states schematics in Fig. 4. At the beginning of the process, the initial condition of the heat pipe is represented by point 1. In this case, as the startup

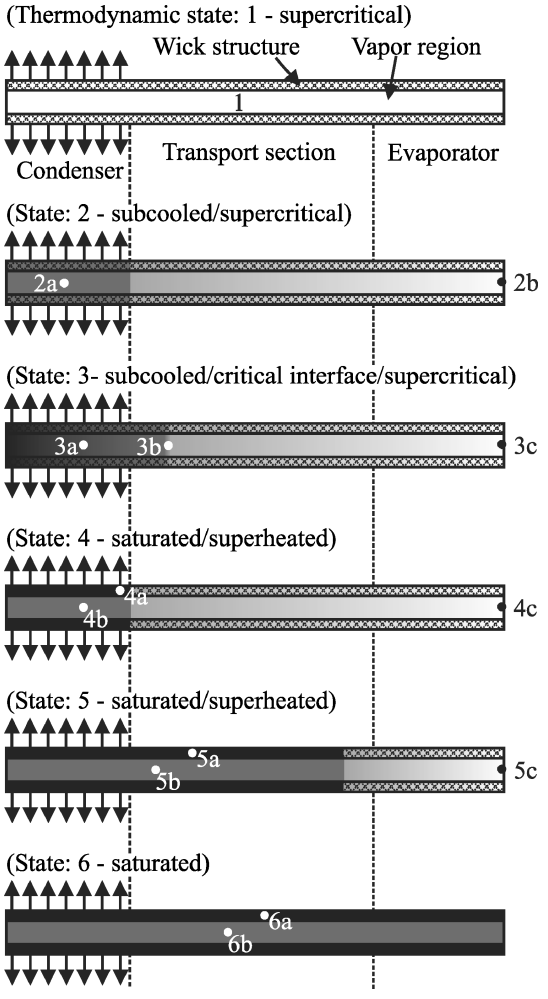

Fig. 4 Thermodynamic state schematics for $v_f < v_{crit}$.

continues the condenser will reach the critical temperature before the vapor pressure decreases below the critical pressure, at point 2a. At this point, the vapor inside the condenser region changes from supercritical fluid to subcooled liquid because its temperature is below the critical temperature, but the vapor pressure is still greater than the critical pressure ($T_c < T_{crit}$ and $P_v > P_{crit}$). The subcooled liquid fills the wick structure and the vapor space in the condenser region, forming a liquid slug. As the temperature of the condenser

decreases, the subcooled liquid slug extends into the transport section until the vapor pressure equals the critical pressure at point 3c. At this point, the leading edge of the subcooled slug will be at a critical condition once the local temperature and vapor pressure are equal to the critical temperature and pressure [$T(x = s - L_c) = T_{\text{crit}}$ and $P_v = P_{\text{crit}}$]. From this point on, the length of the subcooled liquid slug decreases until the condenser temperature reaches the saturation pressure at that point in time [$T_c = T_{\text{sat}}(P_v)$] at point 4a. At this point, the condenser region is filled with saturated working fluid: saturated liquid in the wick structure (point 4a) and saturated vapor in the vapor space (point 4b). The remaining length of the heat pipe remains dry, in a superheated condition. As the temperature of the condenser continues to decrease (line 5a–5b–5c), more liquid is condensed along the wick structure. The process continues until the heat pipe is completely primed, and the thermodynamic state at the wick structure and vapor region is given by points 6a and 6b, respectively.

Thermal Model

The overall thermal model of the supercritical startup of cryogenic heat pipes consists of the following submodels: conduction for the heat pipe wall, liquid column, and internal vapor pressure, all solved for two stages. In the first stage, the heat pipe contains only supercritical vapor, and the primary mechanism of heat transfer is conduction. In this case, a conductive model is used to determine the axial temperature profile. When condensation of working fluid occurs in the condenser region (second stage), a conductive model and a liquid column model are solved together to determine the axial temperature profile and the liquid column length. A vapor pressure model is iteratively used to determine the working fluid pressure. The vapor pressure and temperature at the condenser region are used as parameters to determine the beginning of the condensation process.

Heat-Transfer Model: First Stage

Initially, the heat pipe contains only supercritical vapor and the temperature at the condenser is specified. According to Fig. 1, as the condenser temperature is considered to be uniform at any time t, the origin of the coordinate system used for the modeling of the supercritical startup of cryogenic heat pipes is located at the interface between the condenser and the transport sections. The heat conduction at the dry region of the heat-pipe wall and wick structure is one dimensional, and the thermal conduction through the working fluid is negligible when compared to that through the heat pipe wall. The one-dimensional heat-conduction equation for the physical model presented in Fig. 1 is given by

$$(\rho c)_{\text{eff}} \frac{\partial T}{\partial t} = \frac{\partial}{\partial x}\left(k_s \frac{\partial T}{\partial x}\right) + \frac{\sigma_r \varepsilon A F_{\text{HP},\infty}\left(T_\infty^4 - T^4\right)}{V_s} \tag{1}$$

The second term on the right-hand side of Eq. (1) accounts for the radiative parasitic heat load on the external surface. To account for the heat capacity of the working fluid, Yan and Ochterbeck[17] added to the heat capacity of the solid wall a constant coefficient that accounts for the total change of the internal energy from the initial thermodynamic state to the final thermodynamic state for the heat-pipe wall and the working fluid. This coefficient was defined as

$$\beta = \frac{\Delta E_s + \Delta E_f}{\Delta E_s} \tag{2}$$

and the effective volumetric heat capacity C_{eff} was defined as

$$C_{\text{eff}} = (\rho c)_{\text{eff}} = (1 + \beta)\rho_s c_s \tag{3}$$

where ΔE_s and ΔE_f are the total internal energy change from the initial state to the final state for the heat-pipe wall and the working fluid, respectively.

The initial condition for Eq. (1) is assumed as a constant temperature T_0 for the entire heat-pipe length. The boundary conditions at the interface between the condenser and the transport section are a time-variable temperature given by the cryocooler, while the evaporator end is considered to be insulated:

$$T = T_0 \qquad \text{for} \qquad t = 0 \tag{4}$$

$$T = T_c(t) \qquad \text{for} \qquad x = 0 \tag{5}$$

$$\frac{\partial T}{\partial x} = 0 \qquad \text{for} \qquad x = L \tag{6}$$

Heat-Transfer Model: Second Stage

When the vapor pressure inside the heat pipe equals the saturation pressure at a given condenser temperature [$P_v = P_{\text{sat}}(T_c)$], vapor begins to condense at the wick structure, and a liquid column develops. Saturated liquid flows within the liquid column with an average velocity U. Once the wick structure is filled with saturated liquid, the liquid column will advance in the direction of the evaporator end with a rewetting velocity U_r. At the leading edge of the liquid column, liquid is vaporized because the dry region of the heat pipe is at a higher temperature. Also, the parasitic heat load will vaporize some liquid along the column. If the summation of the parasitic heat load and the heat supplied by the dry region is greater than that heat needed to vaporize the entire advancing liquid column, the rewetting process will stagnate. The total length of the liquid column is s, and its temperature is considered to be uniform and equal to the temperature of the heat-pipe wall. At the condenser, this temperature is equal to the cryocooler temperature. Figure 5 shows the physical model for the supercritical startup considering the rewetting process of the liquid column.

The one-dimensional heat-transfer equation for the dry region of the physical model presented in Fig. 5 [$s(t) - L_c < x < L$] remains that of Eq. (1). However, as the liquid column eventually moves towards the evaporator end, the boundary condition for this stage is considered to be a moving boundary condition at the position $x = s(t) - L_c$, where L_c is the condenser length:

$$T = T_c(t) \qquad \text{for} \qquad x = s(t) - L_c \tag{7}$$

The position of the liquid column can be obtained as a function of time by a heat balance at the leading edge of the liquid column,

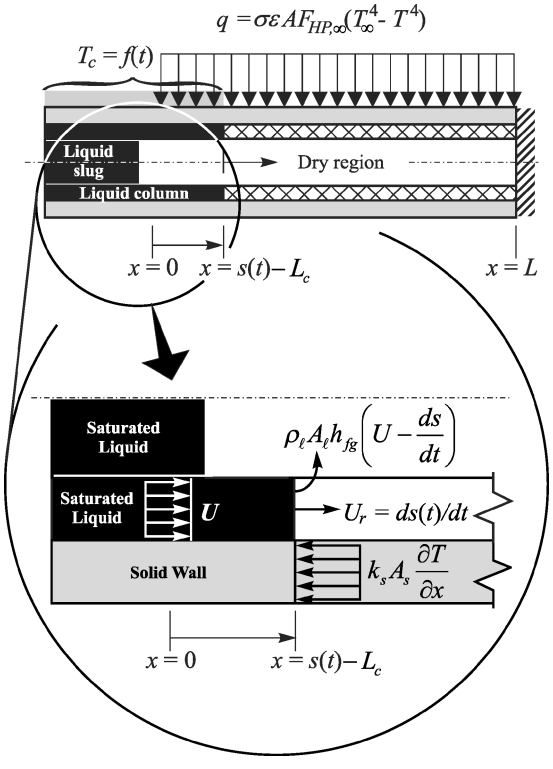

Fig. 5 Physical model and coordinate system.

as follows:

$$\left(k_s A_s \frac{\partial T}{\partial x}\right)_{x=s-L_c} = \left[\rho_\ell A_\ell h_{\text{fg}}\left(U - \frac{\mathrm{d}s}{\mathrm{d}t}\right)\right]_{x=s-L_c} \tag{8}$$

where $\mathrm{d}s/\mathrm{d}t$ is the velocity that the liquid column advances, that is, the rewetting velocity U_r. The initial condition is given as $s = L_c$ at the time that the condensation process of the working fluid begins in the wick structure.

Liquid-Column Model

The liquid column is modeled according to the methodology presented by Ochterbeck et al.[18] In this case, two rewetting processes are considered: the rewetting process of a rectangular groove and the rewetting process of a porous sintered metal wick. A momentum balance is performed at the liquid column, and the total liquid column is taken as the control volume. The advancing liquid column is subjected to a capillary driving force induced by the surface tension and is opposed by the wall shear stress[19]:

$$F_{\text{cap}} - F_{\text{fric}} = \frac{\mathrm{d}(m_\ell U)}{\mathrm{d}t} \tag{9}$$

Model for Axial Grooves

The mathematical solution of Eq. (9) provides an expression for the length of the liquid column and the velocity U as a function of time. As the velocity U is related with the length of the liquid column by $U = \mathrm{d}s/\mathrm{d}t$, the velocity of the liquid inside the column for an unheated surface can be expressed as follows:

$$U = (\sigma h/2\mu_\ell s)[w/(2h + w)]^2 \tag{10}$$

where details about the derivation and solution can be found in Yan and Ochterbeck.[17] The average liquid velocity U obtained from Eq. (10) refers to an unheated groove. The parasitic heat load applied to the heat-pipe wall will cause some working fluid to evaporate from the liquid column. Therefore, a mass balance in the liquid column is performed between $x = 0$ and $x = s(t) - L_c$ to obtain the corrected value for the velocity U at the column leading edge:

$$\frac{\mathrm{d}m_\ell}{\mathrm{d}t} = \dot{m}|_{x=0} - \dot{m}_{\text{evap}} \tag{11}$$

The evaporation mass flux in Eq. (11) is a function of the parasitic heat load, and it provides a relation between the velocity U and the parasitic heat load that affects the liquid column[20]:

$$U = \frac{\sigma h}{2\mu_\ell L_c}\left(\frac{w}{2h + w}\right)^2 - \frac{q''_p[2\pi r_v(s - L_c)]}{\rho_\ell A_\ell h_{\text{fg}}} \tag{12}$$

It is clear that if there is no parasitic heat load Eq. (12) reduces to Eq. (10). Equation (12) is valid for heated axial rectangular grooves.

Model for Porous Sintered Metal Wicks

For porous sintered metal wick structures, the mathematical solution of Eq. (9) provides the following expression for the velocity U as a function of time and length of the liquid column[20]:

$$U = \frac{2\sigma\varphi K^{\frac{1}{2}}}{\mu_\ell s} \tag{13}$$

Correcting the velocity of the liquid column in the porous sintered metal wick structure to account for the effects of the parasitic heat load in the same fashion as used for the axial grooves, the final expression that relates the average velocity of the liquid column and the liquid column position is

$$U = \frac{2\sigma\varphi K^{\frac{1}{2}}}{\mu_\ell s} - \frac{q''_p[2\pi r_v(s - L_c)]}{\rho_\ell A_\ell h_{\text{fg}}} \tag{14}$$

Equation (14) is valid for a heated porous sintered metal wick structure.

Vapor-Pressure Model

The vapor pressure can be obtained by using the following thermodynamic relation:

$$P = \rho_f Z R_g T \tag{15}$$

As the vapor pressure is constant, and as the temperature of the heat pipe varies axially, the specific volume must vary axially so that the conservation of the working fluid mass in the heat pipe is satisfied. Thus, the process to determine the vapor pressure is iterative. First, the heat-pipe length is divided into J finite volumes, and a vapor pressure is guessed for each time step. Equation (15) is then solved for each one of the finite volumes to determine the density of each volume, including the condenser. Then, the mass of fluid in each volume is obtained from $m_j = V_j \rho_j$. The total mass is given by the summation of the mass of each volume:

$$m_f = \sum m_j \tag{16}$$

If the mass obtained from Eq. (16) is different than the real fluid mass of the heat pipe, another pressure is guessed until the mass conservation inside the heat pipe is reached. When the temperature of the condenser T_c is below the critical temperature, the pressure of the heat pipe P is compared to the saturation pressure at the condense temperature $P_{\text{sat}}(T_c)$. If $P = P_{\text{sat}}(T_c)$, then the condensation process begins.

The compressibility factor in Eq. (15) is given by Jacobsen et al.[21] as

$$Z = \frac{P}{\rho R_g T} = 1 + \bar{\rho}\left(\frac{\partial \bar{\alpha}}{\partial \bar{\rho}}\right) \tag{17}$$

where $\bar{\rho}$ is the reduced density (ρ/ρ_{crit}) and $\bar{\alpha}$ is the residual Helmoltz energy, determined by least-square fitting of experimental data. The procedure for the calculation of $\bar{\alpha}$ is fully described by Jacobsen et al.[21] and Stewart et al.[22]

Model Solution

As Eq. (1) is nonlinear in temperature because of the parasitic heat load term, a numerical solution based on the finite volume method[23] was used. The heat-pipe length was divided into J volumes, and Eq. (1) was integrated inside each volume to provide implicit equations for the temperature. After the discretization, the partial nonlinear differential equation is transformed in a system of linear equations, which can be written in a matrix form as follows:

$$[\boldsymbol{T}|_{t-\Delta t}] = [\boldsymbol{a}][\boldsymbol{T}|_t] + [\boldsymbol{b}] \tag{18}$$

where the matrix $[\boldsymbol{T}|_t]$ is unknown. The solution is found from

$$[\boldsymbol{T}|_t] = [\boldsymbol{a}]^{-1}\{[\boldsymbol{T}|_{t-\Delta t}] - [\boldsymbol{b}]\} \tag{19}$$

The numerical solution allows the thermophysical properties of the heat-pipe wall to be considered as a function of the local wall temperature. The thermophysical properties of the saturated working fluid are considered to be a function of the condenser temperature and are found in Jacobsen et al.[21]

For the first stage of the startup process, the system given by Eq. (19) is solved together with boundary conditions (3) and (4) until the temperature at the condenser reaches T_{sat}, when the condensation process begins (second stage). For the second stage of the startup process, Eqs. (12) and (14) (depending on the wick structure geometry) are used to determine U. Then, Eqs. (8) and (19) are solved iteratively to determine the temperature profile and the position of the liquid column. The solution of the model is performed until the liquid column reaches the evaporator end ($s = L$, operational steady-state condition), or until the temperature at the evaporator end varies less than 1 K/h, for a liquid column length smaller than the heat-pipe's length (nonoperational steady-state condition). Once the temperature profile of the heat pipe is determined, Eqs. (15) and (16) are solved to determine the pressure and the mass distribution of the working fluid.

Model Validation

For the validation of the model, the experimental data of two aluminum/oxygen cryogenic heat pipe presented by Brennan et al.[15] and one titanium/nitrogen cryogenic heat pipe presented by Rosenfeld et al.[16] were used. The parameters are shown in Tables 1 and 2.

For an accurate solution of the model, the $\varepsilon F_{\mathrm{HP},\infty}$ term to be used during the evaluation of the parasitic heat load in Eq. (1) must be determined. Brennan et al.[15] estimated the parasitic heat load to be from 1.1 to 1.9 W, when the heat pipe was isothermalized around 60 K. Therefore, the term $\varepsilon F_{\mathrm{HP},\infty}$ can be found by using the relation

$$q_p = \sigma_r \varepsilon F_{\mathrm{HP},\infty} A_e \left(T_\infty^4 - T_{\mathrm{HP}}^4\right) \tag{20}$$

The following assumptions are considered:

1) The heat pipe is isothermalized at $T_{\mathrm{HP}} = 60$ K.

2) The surrounding temperature T_∞ is constant with time and is equal to the initial temperature of the heat pipe T_0 (280 K).

3) The term $\varepsilon F_{\mathrm{HP},\infty}$ is considered to be constant with temperature.

For the TRW heat pipe, the $\varepsilon F_{\mathrm{HP},\infty}$ was obtained for the two extreme parasitic heat loads estimated by Brennan et al.[15] An average value of 1.5 W was also considered. For the Hughes Aircraft Corporation (HAC) heat pipe, the parasitic heat load of 1.14 W was used. No information regarding the parasitic heat load was presented by Rosenfeld et al.[16] for the nitrogen heat pipe (NHP) heat pipe. Therefore, an average value of the Thompson-Ramo-Wooldrige (TRW) Inc., (TRW) and HAC parasitic heat load ($q_p = 1.48$ W) was used to calculate the $\varepsilon F_{\mathrm{HP},\infty}$ term for the temperature range of 285 to 75 K. Table 3 presents the estimated values.

Results for the TRW Heat Pipe

Figure 6 shows the comparison between the theoretical model and the experimental flight data for the TRW aluminum/oxygen cryogenic heat-pipe startup. The temperature at the condenser (boundary condition) was obtained by fitting a sixth-order polynomial to the experimental data of the cryocooler. The overall agreement between the model and the experimental data is good. However, the model slightly underestimates the temperatures at the evaporator end. Some possible reasons for this deviation are listed here:

1) The first reason is inadequate estimation of the parasitic heat load. Brennan et al.[15] had not specified whether the parasitic heat load was radiative or (and) conductive.

2) The capillary radius of the liquid column was not considered for the calculation of the liquid column momentum [Eq. (9)]. If the curvature of the free surface was taken into account, the area of the liquid would be smaller, and consequently the mass of the liquid column would decrease.

Figure 7 shows the pressure-specific volume diagram for the supercritical startup of the TRW cryogenic heat pipe. The specific

Table 1 Aluminum/Oxygen Heat Pipes Design Summary (Brennan et al.[15])

Design Parameter	TRW	HAC
Tube material:	Aluminum Alloy, 2024-T6	
Tube dimensions:		
Outer diameter	11.2 mm	15.91 mm
Vapor diameter	7.37 mm	8.64 mm
Wall thickness	1.02 mm	2.54 mm
Lengths:		
Evaporator	0.15 m	0.15 m
Condenser	0.15 m	0.15 m
Transport section	1.02 m	1.07 m
Oxygen charge	10.3 g	33.7 g
Number of Grooves	17	27
Groove width	0.445 mm	0.658 mm
Fin Fip Radius	0.102 mm	0.16 mm
Wetted Perimeter (1 Groove)	2.09 mm	3.25 mm
Total Groove Area	6.07 mm^2	23.2 mm^2

Table 2 Titanium/Nitrogen Heat pipe Design Summary (Rosenfeld et al.[16])

Design Parameter	NHP
Tube material:	Titanium Alloy, Ti-6Al-4V
Tube dimensions:	
Outer diameter	15.0 mm
Wall thickness	1.026 mm
Lengths:	
Evaporator	0.127 m
Condenser	0.178 m
Transport section	0.613 m
Nitrogen charge	24.1 g
Number of metal cables	6
Cable material	Fibrous copper
Cable diameter	3.20 mm
Porosity[a]	0.520 to 0.895[b]
Permeability $\times 10^{10}$[a]	0.009 to 12.4 m^2[b]

[a]Not available in Rosenfeld et al.[16]

[b]Typical values from the literature (Faghri[24]).

Table 3 Estimated values for $\varepsilon F_{\mathrm{HP},\infty}$

q_p (W)	Heat Pipe	$\varepsilon F_{\mathrm{HP},\infty}$
1.10	TRW	0.077
1.50	TRW	0.104
1.90	TRW	0.134
1.48	NHP	0.114
1.14	HAC	0.056

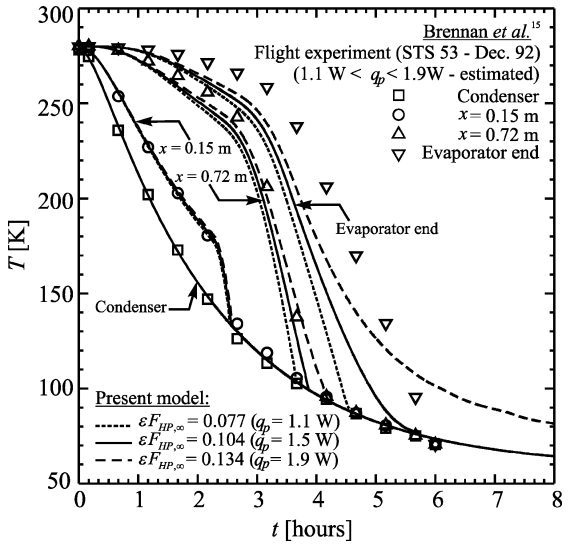

Fig. 6 Comparison between the theoretical model and the experimental data.

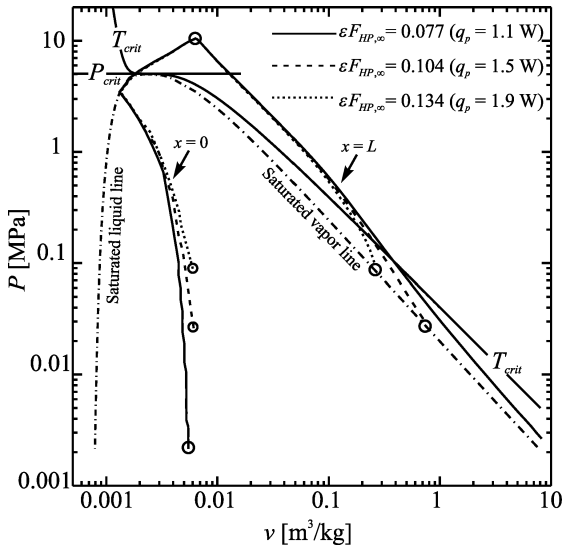

Fig. 7 Pressure-specific volume diagram (TRW heat pipe).

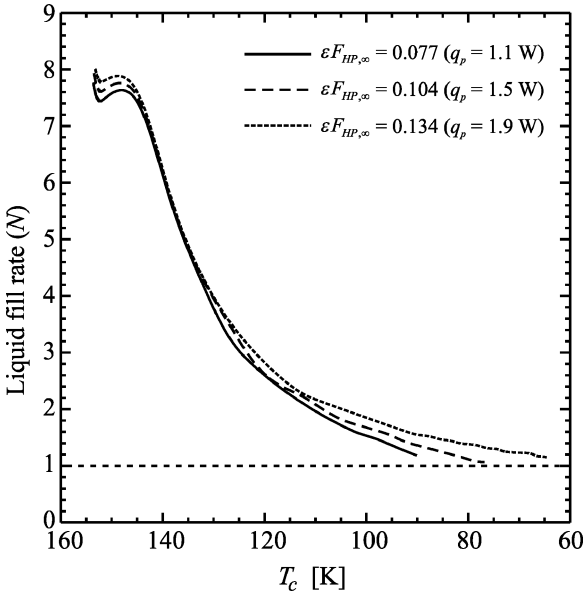

Fig. 8 Liquid fill rate.

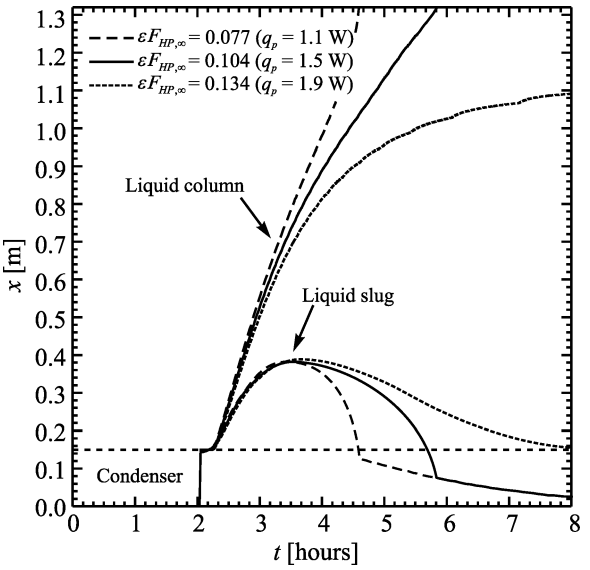

Fig. 9 Predicted liquid front and liquid slug position (TRW).

volume is shown at the interface between the condenser and transport section ($x = 0$) and for the evaporator end ($x = L$). The condensation process will begin at $T_{\text{sat}} = 153.6$ K. Also, the condensation begins from the saturated liquid line. It means that for a short period of time (for less than 2 min), the condensed liquid in the condenser region will be in a subcooled condition. After the condensation process begins, the quality at the condenser remains closer to zero until the liquid column starts to move towards the evaporator end. This is because more liquid is being condensed as the temperature of the condenser decreases.

The liquid fill as a function of the temperature of the condenser is shown in Fig. 8. The liquid fill is defined as the ratio between the condensed liquid mass m_ℓ and the mass that the wick structure can hold m_w:

$$N = \frac{m_\ell}{m_w} = \frac{(1-n)A_c s/v_c}{A_w s/v_\ell} \tag{21}$$

where A_c is the cross-sectional area of the condenser (liquid + vapor) and A_w is the cross-sectional area of the grooves. If $N = 1$, the mass of liquid is enough to fill the grooves with no excess liquid. For $N > 1$ there is excess liquid. As seen, there is a large excess of liquid when the startup process begins. This is because the oxygen enters the saturation zone from a subcooled condition. Therefore, the condenser is flooded with saturated liquid. The fill rate starts to decrease as the liquid column begins to advance and as the liquid specific volume decreases with continued decrease in temperature.

Figure 9 shows the position of the liquid column inside the axial grooves as a function of time. Also the position of the liquid slug is shown. This slug was observed by Brennan et al.[15] and only occurs in microgravity environment. On the ground, the capillary forces cannot support a slug across the vapor region, and excess of liquid is spread as a puddle.[15] This effect facilitated the priming of a heat pipe in ground tests. As shown in Fig. 9, when the startup process begins the liquid column remains stagnated at the interface between the condenser and the transport region for a few minutes (12.5 min.). This is because the liquid velocity in the liquid column is not sufficient to provide the cooling to the dry region of the heat pipe. As the temperature of the condenser decreases, the surface tension of the working fluid increases, which increases the capillary driving force. Also, with time, the region next to the liquid column is cooled by conduction, thus lowering the local wall temperature and heat flux to the front of the liquid column. So, the liquid column will eventually advance towards the evaporator end. For a lower parasitic heat load (1.1 W), the startup process was faster because less fluid was evaporated from the liquid column. For a higher parasitic heat load (1.9 W), the analytical model shows that the heat pipe would not prime completely, with the liquid column stagnating at about 0.21 m from the evaporator end.

The position of the slug was determined from the data shown in Fig. 8, for $N > 1$. The position of the liquid slug increases with time until it reaches a maximum at about 0.40 m from the condenser end, and then it decreases. The rate of change of the liquid slug position relative to time ($\mathrm{d}s/\mathrm{d}t$) changes when the heat pipe is fully primed (at 4.6 h for 1.1 W, and at 5.9 h for 1.5 W). This is because the liquid slug length is driven by two factors when the heat pipe is not yet fully primed: 1) saturated liquid is removed from the slug to supply the liquid column inside the wick structure, and 2) saturated liquid turns into saturated vapor at the leading edge of the liquid slug because of the thermodynamic state of the heat pipe (vapor pressure and temperature). When the heat pipe is fully primed, no more liquid is removed from the liquid slug to the liquid column once the wick structure is completely primed with saturated liquid. Then, the length of the liquid slug is determined only by the thermodynamic state of the heat pipe. As the temperature of the heat pipe continues to decrease (and consequently, the vapor pressure), the liquid slug length decreases, and it tends to zero as the heat-pipe temperature tends to 60 K. This because the mass of 10.3 g of oxygen on the TRW heat pipe was designed to completely fill the wick structure with saturated liquid with no excess at 60 K. If the TRW heat pipe works in a temperature above 60 K in microgravity environment, the liquid slug will block part of the condenser region. For example, if the operating temperature is 90 K, there is an excess of liquid of 1.8 g, which provides a slug that is almost 0.2 m long, blocking completely the condenser region. At about 75 K the slug length is 0.12 m from the condenser end.

Results for the HAC Heat Pipe

Figure 10 shows the comparison between the theoretical model and the experimental data for the HAC[16] aluminum/oxygen cryogenic heat-pipe startup. The temperature at the condenser (boundary condition) was obtained by fitting a third-order exponential decay function to the experimental data of the cryocooler. The model and data comparison is good for the heat-conduction model (first stage of the startup process).

The condensation of the working fluid started at a temperature far below the oxygen critical temperature (154.6 K), around 128 K. This is because the vapor pressure only drops below the critical pressure when the condenser temperature drops below 128 K. This phenomenon is better observed by analyzing Fig. 11, which presents a pressure-specific volume diagram for the supercritical startup of the oxygen/aluminum HAC heat pipe.

The supercritical startup process of the HAC heat pipe starts at 285 K, at a pressure around 20 MPa (point 1 in Fig. 11—the number

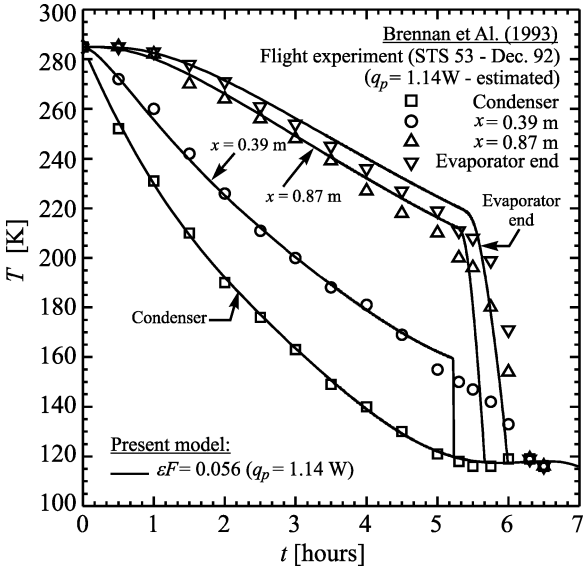

Fig. 10 Comparison between the theoretical model and the HAC experimental data.

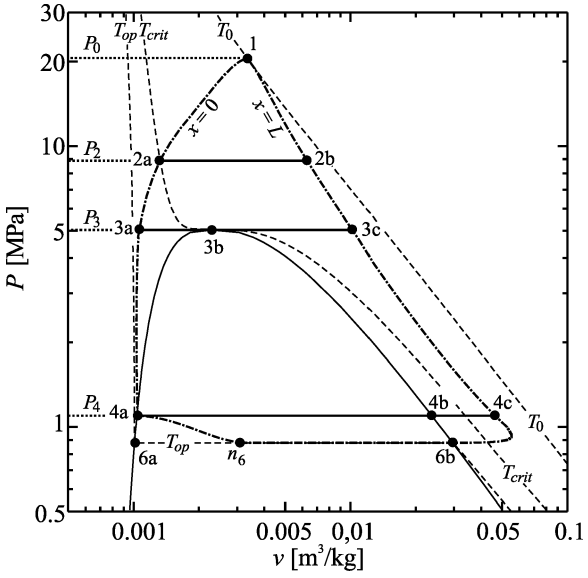

Fig. 11 Pressure-specific volume diagram (HAC heat pipe).

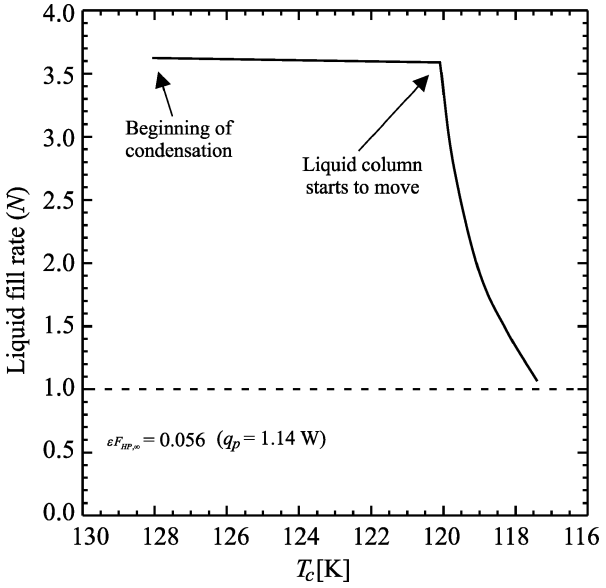

Fig. 12 Liquid fill rate (HAC heat pipe).

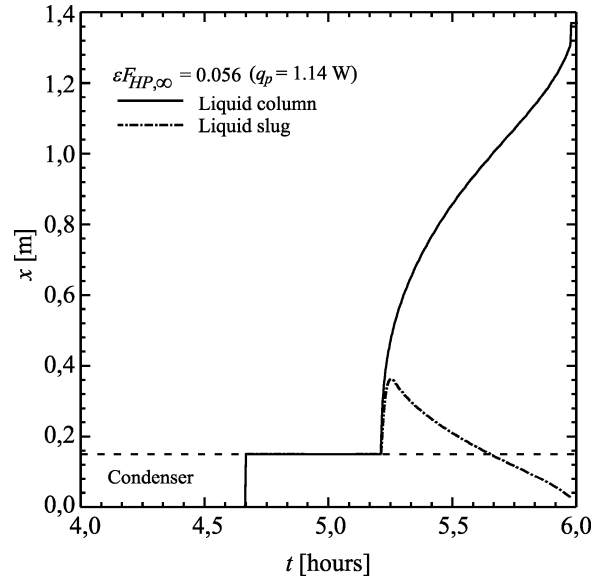

Fig. 13 Predicted liquid slug and liquid front position (HAC heat pipe).

of the points in this figure agree with those in Fig. 3). As the condenser cools down, the vapor pressure decreases. When the condenser cools to a temperature equal to the oxygen critical temperature ($T_{\text{crit}} = 154.6$ K) at point 2a, the pressure of the working fluid inside the heat pipe is still greater than the oxygen critical pressure ($P_2 = 8953$ kPa $> P_{\text{crit}} = 5043$ kPa). As the condenser continues to cool down, a subcooled liquid slug is formed in the condenser region of the heat pipe. When the pressure of the working fluid equals the oxygen critical pressure, the temperature at the condenser end is 128 K (point 3a). At this point in time, the subcooled liquid slug extended for 0.17 m in the adiabatic section of the HAC heat pipe (point 3b). As the startup process continues, the subcooled liquid slug recedes until the condenser is completely filled with saturated working fluid at a temperature of 122 K. At this point, the working fluid pressure equals the saturation pressure at 122 K, and the rewetting process starts. The thermodynamic condition of the saturated liquid in the wick structure is given by point 4a and the saturated vapor in the vapor region, by point 4b. The remaining length of the heat pipe (line 4b–4c) is at a superheated condition. According to Fig. 10, the theoretical rewetting process is faster than the experimental process presented by Brennan et al.[15] This is because at 120 K the capillary forces developed at the grooves of the HAC heat pipe are large enough to drive the saturated liquid column towards the evaporator end. As the liquid column starts to advance, more vapor is condensed, decreasing the specific volume of the superheated vapor at the evaporator end as shown by the line that connect points 4c and 6b in Fig. 11. The heat pipe reached an operational steady state at 117.5 K after 6 h of the beginning of the startup process.

The liquid fill rate, obtained from Eq. (21), of the HAC heat pipe is shown in Fig. 12. It can be observed that there is an excess of liquid of almost 350% at the beginning of the condensation process. As the liquid column starts to move, the liquid fill rate decreases, achieving a value next to the unit ($N = 1$) in steady state. From the liquid fill rate data, it is possible to determine the length of the liquid slug observed by Brennan et al.[15] Figure 13 shows the liquid slug and liquid column position as a function of the startup time.

Results for the Nitrogen Heat Pipe

The titanium/nitrogen heat pipe (NHP) tested by Rosenfeld et al.[16] did not reach an operational steady state, with just 32% of the total heat-pipe length cooling below the critical temperature of nitrogen (126.2 K). Although little information regarding the parasitic heat load and the wick structure of this heat pipe is available at Rosenfeld et al.,[16] the experimental data for this unsuccessful startup can be used for comparison with the presented model, and some

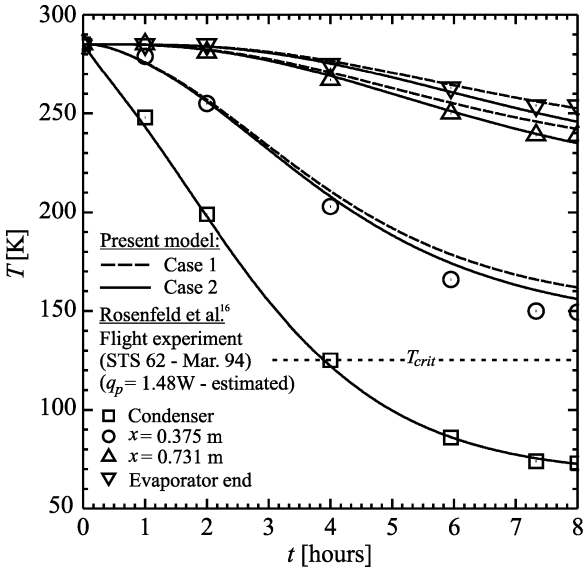

Fig. 14 Comparison between the theoretical model and the NHP experimental data.

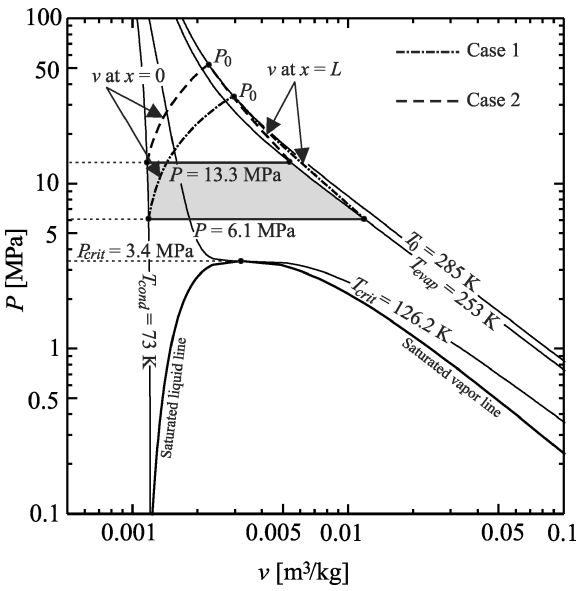

Fig. 15 Pressure-specific volume diagram (NHP heat pipe).

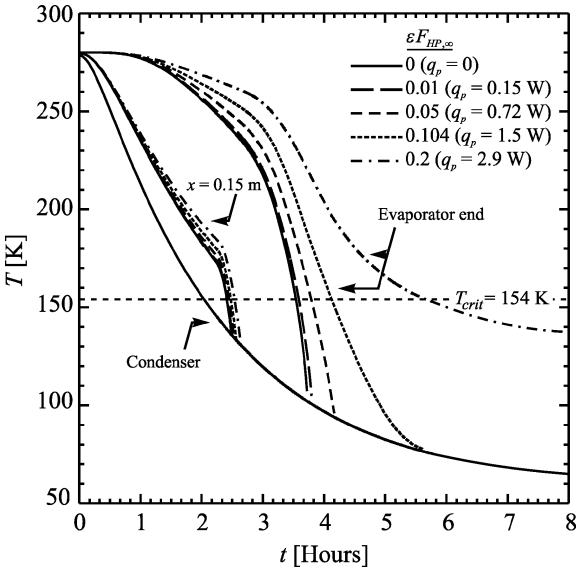

Fig. 16 Effects of the parasitic heat load.

conclusions can be drawn regarding the titanium/nitrogen heat pipe. The wick structure of the NHP was composed by six porous copper cables with a circular section of 3.2 mm of diameter held against the internal diameter of the titanium alloy (Ti-6 Al-4V ELI) pipe by a full-length centered spring. The authors presented no values for the porosity and permeability, but typical values can be found in the literature (Faghri[24]): $0.520 \leq \varphi \leq 0.895$ and $0.009\ \text{m}^2 \leq K \leq 12.4\ \text{m}^2$ ($\times 10^{-10}$). According to Eq. (14), which gives an average velocity of the saturated liquid in a porous wick structure, the combination of φ and K that produces the largest velocity is $\varphi = 0.895$ and $K = 12.4 \times 10^{-10}\ \text{m}^2$. Also, the largest porosity provides more void volume in the wick structure to be filled with liquid, and therefore it provides a lower vapor pressure during startup if compared to a lower porosity. So, the two extremes of cable properties were considered for comparison with the experimental data—case 1: $\varphi = 0.895$ and $K = 12.4 \times 10^{-10}\ \text{m}^2$; and case 2: $\varphi = 0.520$ and $K = 0.009 \times 10^{-10}\ \text{m}^2$.

Figure 14 presents the comparison between the experimental data of Rosenfeld et al.[16] and the theoretical model. The temperature at the condenser (boundary condition) was obtained by fitting a third-order exponential decay function to the experimental data of the cryocooler. The comparison is good, and the model predicted the unsuccessful startup of the titanium/nitrogen heat pipe. This failure is because the vapor pressure never reached the critical pressure of the nitrogen in none of the cases, even though the temperature of the condenser was far below the critical temperature of the nitrogen even after 8 h of testing. The pressure-specific volume diagram for the NHP is shown in Fig. 15 for both cases. Although the mass charge is fixed for both cases, the initial condition given by P_0 is different because the porosity is different for each case, which causes the void volume to be different. Consequently, the specific volume of the working fluid (void volume/working fluid mass) is also different for each case. It can be observed that, for the largest porosity (case 1), the vapor pressure at steady state reached 6.1 MPa, whereas for the lower porosity the pressure at steady state was 13.3 MPa (more than twice larger!). However, in both cases the steady-state pressure was still higher than the critical pressure of the nitrogen (3.4 MPa), and therefore no condensation of the working fluid occurred during the startup because a saturated thermodynamic condition was never reached in the titanium/nitrogen heat pipe. The shaded zone in Fig. 15 represents any steady state possible for the combination of porosity and permeability within the typical ranges for porous metal wick structures.

Concluding, the nonoperational steady state reached by the titanium/nitrogen heat pipe was caused by a combination of the effects of the parasitic heat loads, low conductance of the titanium wall, and mass of working fluid. The designed working fluid mass of 24.1 g provided a high initial pressure, and the low conductance of the heat pipe wall, added to the parasitic heat load, did not provide enough cooling for the vapor pressure to decrease below the critical pressure of the nitrogen.

Startup Limitation Analysis

The startup limitation for an axially grooved cryogenic heat pipe is now discussed based on the theoretical results given by the model presented. The analysis will focus on the effects of the parasitic heat load over the temperature profile and liquid column length, as well as the effects of some geometrical parameter, and working fluid charge. The TRW heat pipe[15] is considered here. All of the geometric parameters were kept equal to those shown in Table 1, except when specified.

Figure 16 shows the effect of the parasitic heat load over the temperature of the heat pipe. The figure shows different transient temperatures for different values of $\varepsilon F_{\text{HP},\infty}$. The number inside the brackets in the legend refers to the corresponding parasitic heat load, for an isothermal heat pipe at 60 K, with the same geometry of the TRW heat pipe. Temperatures are shown for three different positions: $x = 0$ (condenser), $x = 0.15$ m (inside the transport section), and $x = L$ (evaporator end).

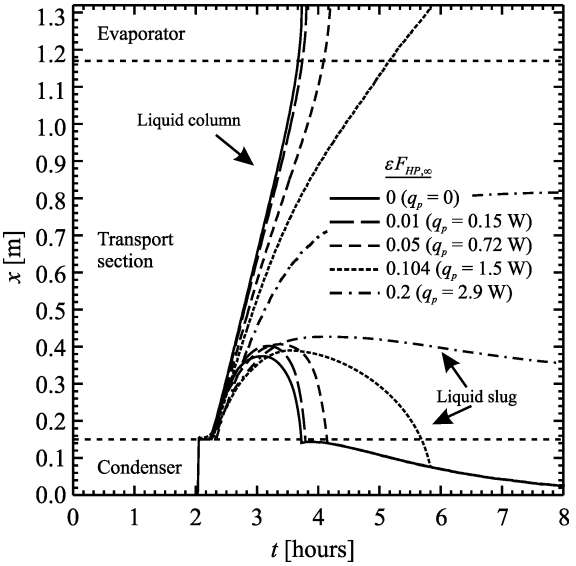

Fig. 17 Liquid column length.

As expected, the priming of the heat pipe is slower as the parasitic heat load increases. It appears that the TRW heat pipe is almost at the edge of the parasitic heat load. It primed for a parasitic heat load of 1.5 W, but did not for a parasitic heat load of 1.9 W and above (see Figs. 6 and 9). The TRW heat pipe was specifically designed to have a low transport capability such that data could be obtained for analytical model validation.[15]

The position of the liquid column and liquid slug as a function of the startup time is shown in Fig. 17. If there is no parasitic heat load, the heat pipe will prime completely in 3.67 h. The time that the liquid column stays stagnated in the interface between the condenser and the transport section is 11 min for no parasitic heat load and up to 15 min for 2.9 W. In the later case, only 0.82 m of the heat pipe could be primed. In this same figure, the behavior of the liquid slug is observed for different parasitic heat loads. As the parasitic heat load increases, the maximum length achieved by the liquid slug increases. Also, the rate of change of the liquid slug position relative to time decreases for a larger parasitic heat load, that is, the condenser region remains blocked by the liquid slug for a longer time, even if the heat pipe is fully primed. For example, for a parasitic heat load of 0.72 W the TRW heat pipe will prime in almost 4 h, at a condenser temperature close to 100 K. On the other hand, at 100 K the liquid slug length is almost 0.15 m, blocking the condenser region completely. For a parasitic heat load of 1.5 W, the heat pipe will prime in 5.9 h, at a condenser temperature of 75 K, which corresponds to a liquid slug length of 0.12 m, partially blocking the condenser region.

The effect of the cross-sectional area of the groove on the temperatures of the heat pipe is given in Fig. 18. The aspect ratio for all groove ateas presented in this figure is constant and equal to the aspect ratio of the TRW heat pipe ($h/w = 1.8$). Figure 19 shows the position of the liquid column and liquid slug for the three groove areas presented in Fig. 18. For the largest groove area, the startup time was 4.17 h. For the smallest groove area, steady state was not reached even after 8 h form the beginning of the startup.

Figure 20 shows the transient temperature behavior of the TRW heat pipe during the supercritical startup for different working fluid charge. It can be observed that, as the excess of working fluid increases, the beginning of the condensation process is delayed. The delay on the beginning of the condensation process can be clearly explained by observing Fig. 21, which shows the pressure-specific diagram for the TRW heat pipe for different working fluid charges. A larger working fluid mass will cause a higher initial vapor pressure for a given heat pipe (in this case, the TRW device), as shown in Table 4. Therefore, the heat pipe will reach the critical temperature of the working fluid at a higher pressure (similarly to the HAC heat pipe). For a 10.3 g of fluid charge, the vapor pressure at 154.6 K (critical temperature of oxygen) is 5.2 MPa, whereas for 15.45 g (50% of excess) the vapor pressure at the same temperature is 7.5 MPa. The condensation process can only start if both pressure and temperature are below the critical point. For a working fluid mass of 10.3 g, the vapor pressure will decrease below 5.043 MPa (critical pressure of oxygen) only at $T_c = 153$ K, whereas for 15.45 g only at $T_c = 136$ K. At this point, although the vapor pressure and temperature are below the critical point, the liquid column is still in a subcooled thermodynamic condition because the vapor pressure is higher than the saturation pressure at that temperature. As the condenser temperature continues to decrease, the vapor pressure will decrease until the saturation of the liquid column is reached at 150 K for 10.3 g and at 99 K for 15.45 g. Then, the rewetting process

Table 4 Initial pressure at 280 K for the TRW heat pipe

m_f (g)	v_f [a] (m^3/kg)	P_0 (MPa)
10.30[b]	0.006462	10.4
11.33	0.005875	11.4
12.36	0.005385	12.5
15.45	0.004308	15.5

[a] $v_f = V_{\text{void}}/m_f$, where V_{void} is the void volume of the TRW heat pipe (6.65×10^{-5} m^3).
[b] TRW designed working fluid mass.

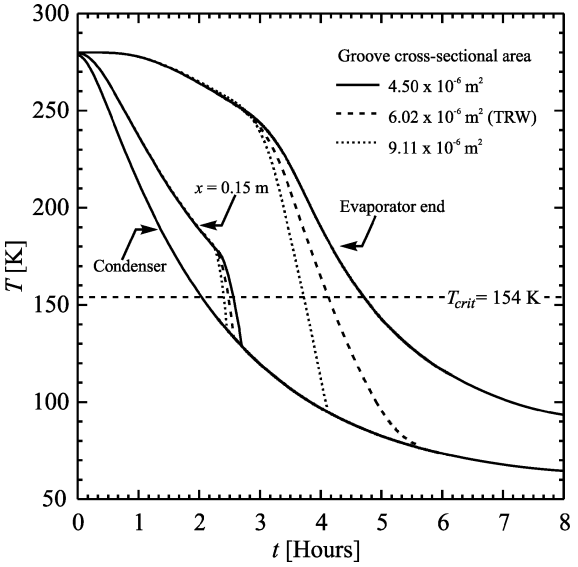

Fig. 18 Effects of groove cross-sectional area.

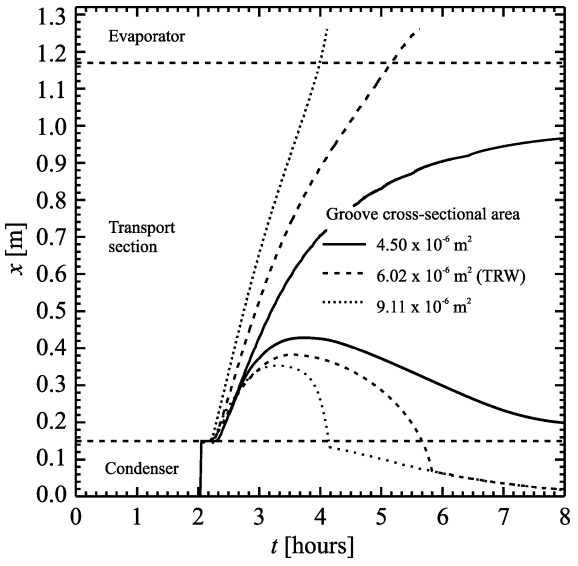

Fig. 19 Liquid column length.

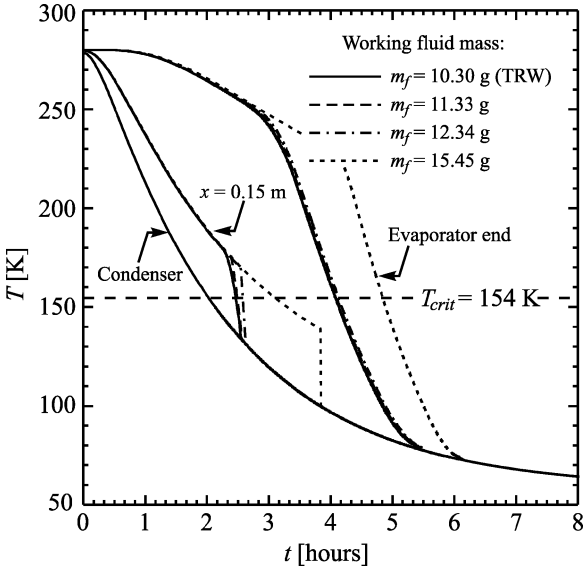

Fig. 20 Effects of the heat-pipe working fluid charge.

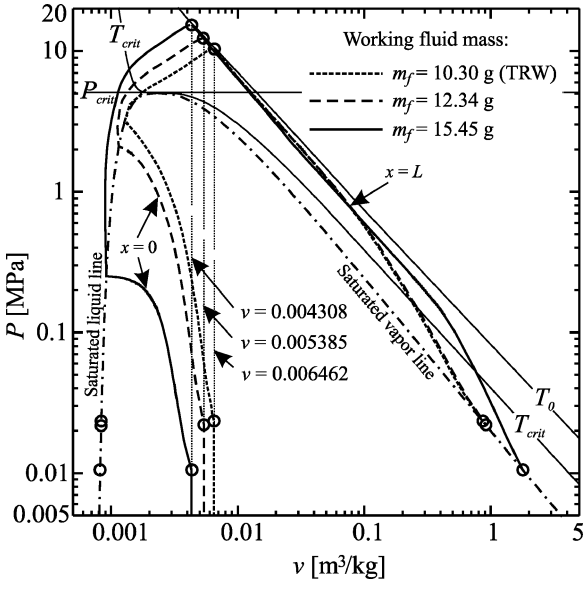

Fig. 21 Pressure-specific volume diagram.

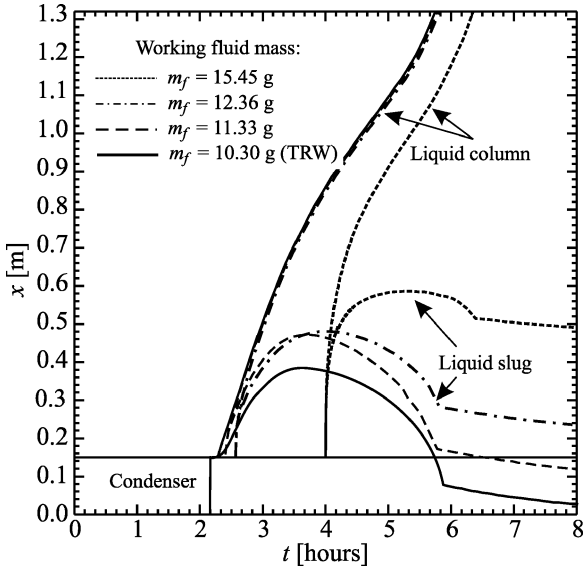

Fig. 22 Liquid-column length.

starts. Figure 22 shows the liquid column and liquid slug positions as a function of time.

Summary

An improved model for the supercritical startup of cryogenic heat pipes was presented. The model included the effects of parasitic heat loads for the entire length of the heat pipe. Also, a methodology for determining the vapor pressure and the mass distribution in the heat pipe was developed. This methodology allowed the determination of the length of the liquid column and the length of the liquid slug.

The presented model compared well with microgravity experimental data available in the literature for axially grooved cryogenic heat pipes. An analysis of the supercritical startup limitation of an axially grooved cryogenic heat pipe in a microgravity environment was performed based on the results obtained from the improved model. The results are summarized next:

1) The parasitic heat load plays an important role in the startup process of cryogenic heat pipes. The parasitic heat loads increases the temperature gradient in the dry region, increasing the vaporization of liquid at the leading edge of the liquid column. Also, the parasitic heat load will vaporize liquid along the length of the liquid column once it starts to advance towards the evaporator.

2) A longer condenser will facilitate the priming process as it allows a larger condensation mass rate.

3) Larger cross-sectional areas of the grooves also help the priming process to occur.

4) An increase of the working fluid charge will increase the vapor pressure of the heat pipe delaying the fluid condensation process. Also, the excess of working fluid will block partially (or completely) the condenser region, decreasing the heat-pipe performance. The combination of the effects of the parasitic heat loads and working fluid excess can cause a nonoperational steady state (failure to startup), as experienced by Rosenfeld et al.[16]

Acknowledgments

The authors would like to acknowledge the help of Y. H. Yan during the development of this work. Couto and Mantelli would like to acknowledge the Brazilian Space Agency (AEB), CAPES Foundation, and the Brazilian Council of Research and Development (CNPq) for supporting this project.

References

[1]Couto, P., "Development and Design of Passives Cryogenic Radiators for Spacecraft Applications," M. Sc. Thesis (original version in Portuguese), Mechanical Engineering Dept., Federal Univ. of Santa Catarina, Florianópolis, SC, Brazil, July 1999.

[2]Brand, O., and Schlitt, R., "Low Temperature Radiator Design for the ABRIXAS X-Ray Satellite," *Proceedings of the 6th European Symposium on Space Environmental Control Systems*, Noordwijk, The Netherlands, 1997, pp. 151–159.

[3]Wright, J. P., "Development of a 5 W 70 K Passive Radiator," AIAA Paper 80-1512, July 1980.

[4]Wright, J. P., and Pence, W. R., "Development of a Cryogenic Heat Pipe Radiator for a Detector Cooling System," American Society of Mechanical Engineers, Paper 73-ENAs-47, July 1973.

[5]Zelenov, I. A., Poskonin, U. A., Timofeev, V. N., Kostenko, V. I., Ribkin, B. I., Romanovsky, O. I., Sidorenko, E. M., and Guskov, A. S., "Flexible Low Temperature and Cryogenic Heat Pipes for the Space Controlled Radiator-Emitter," *Proceedings of the 8th International Heat Pipe Conference*, 1992, pp. E-P66/1–4.

[6]Voyer, E., Moschetti, B., Briet, R., Alet, I., and Evin, R., "Heat Pipes for Cryogenic Applications on Satellites," Society of Automotive Engineers, Technical Paper 972450, July 1997.

[7]Abrosimov, A., Baryshev, O., Horonenko, V., Kosorotov, M., Lobanov, A., and Parfentiev, M., "Diode Cryogenic Heat Pipe for 'SODART' Telescope Silicon Detector Cooling," *Proceedings of the 8th International Heat Pipe Conference*, 1992, pp. E-P54/1–4.

[8]Ishigohka, T., Hirayama, Y., Ninomiya, A., and Maezawa, S., "Conduction Cooling of High-TC Superconducting Magnet Using Heat Pipe," *Proceedings of the 11th International Heat Pipe Conference*, 1999, pp. 139–144.

[9]Couto, P., and Mantelli, M. B. H., "Cryogenic Heat Pipe—A Review of the State-of-the-Art," *Proceedings of the Brazilian Congress of Thermal Engineering and Sciences*, [CD-ROM], Brazilian Association of Mechanical Sciences, Rio de Janeiro, Brazil, 2000.

[10]*PNAE–Brazilian Policy for Space Activities* (original in Portuguese), Brazilian Space Agency, Brasilia, DF, Brazil, 1996.

[11]Peterson, G. P., and Compagna, G. L., "Review of Cryogenic Heat Pipes," *Journal of Spacecraft*, Vol. 24, No. 2, 1987, pp. 99, 100.

[12]Barron, R. F., *Cryogenic Systems*, 2nd ed., Oxford Univ. Press, New York, 1985, pp. 3–55.

[13]Chi, S. W., and Cygnarowicz, T. A., "Theoretical Analyses of Cryogenic Heat Pipes'," American Society of Mechanical Engineers, Paper 70-HT/SpT-6, 1970.

[14]Colwell, G. T., "Prediction of Cryogenic Heat Pipe Performance," NASA Final Report NSG-2054, March 1977.

[15]Brennan, P. J., Thienel, L., Swanson, T., and Morgan, M., "Flight Data for the Cryogenic Heat Pipes (CRYOHP) Experiment," AIAA Paper 93-2735, July 1993.

[16]Rosenfeld, J. H., Buchko, M. T., and Brennan, P. J., "A Supercritical Startup Limit to Cryogenic Heat Pipes in Microgravity," *Proceedings of the 9th International Heat Pipe Conference*, Vol. 2, 1995, pp. 742–753.

[17]Yan, Y. H., and Ochterbeck, J. M., "Analysis of Supercritical Startup Behavior for Cryogenic Heat Pipes," *Journal of Thermophysics and Heat Transfer*, Vol. 13, No. 1, 1999, pp. 140–145.

[18]Ochterbeck, J. M., Peterson, G. P., and Ungar, E. K., "Depriming/Rewetting of Arterial Heat Pipes: Comparison with Share-II Flight Experiment," *Journal of Thermophysics and Heat Transfer*, Vol. 9, No. 1, 1995, pp. 101–108.

[19]Peterson, G. P., *An Introduction to Heat Pipes—Modeling, Testing and Applications*, 1st ed., Wiley, New York, 1991.

[20]Couto, P., "Theoretical and Experimental Analysis of Supercritical Startup of Cryogenic Heat Pipes," Ph.D. Dissertation, Mechanical Engineering Dept., Federal Univ. of Santa Catarina, Florianópolis, Brazil, March 2003.

[21]Jacobsen, R. T., Penoncello, S. G., and Lemmon, E. W., *Thermodynamic Properties of Cryogenic Fluids*, Plenum, New York, 1997.

[22]Stewart, R. B., Jacobsen, R. T., and Wagner, W., "Thermodynamic Properties of Oxygen from the Triple Point to 300 K with Pressures to 80 MPa," *Journal of Physical and Chemical Reference Data*, Vol. 20, No. 5, 1991, pp. 917–1021.

[23]Patankar, S. V., *Numerical Heat Transfer and Fluid Flow*, Hemisphere, Washington, DC, 1980.

[24]Faghri, A., *Heat Pipe Science and Technology*, 1st ed., Taylor and Francis, Washington, DC, 1995, pp. 130–132.